Chemical Engineering Science 310 (2025) 121513

Contents lists available at ScienceDirect

Chemical Engineering Science

journal homepage: www.elsevier.com/locate/ces

Numerical assessment of flow uniformity and recirculation in a water electrolysis cell with knitted mesh and foam-like electrodes

Kevin Van Droogenbroek [a], Christos Georgiadis [a], Benoit Scheid [b], Joris Proost [a,*]

[a] Division of Materials and Process Engineering, Université catholique de Louvain, Louvain-la-Neuve, Belgium
[b] Transfers, Interfaces and Processes, Université Libre de Bruxelles, Brussels, Belgium

ARTICLE INFO

Keywords:
Water electrolysis
Porous transport layer
Residence Time Distribution
Flow uniformity
Flow recirculation

ABSTRACT

In this work, single-phase Computational Fluid Dynamics (CFD) simulations are used to extract, based on a Residence Time Distribution (RTD) analysis, two representative parameters that allow to quantify electrolyte flow uniformity and flow recirculation in water electrolysis cells. This then allows to compare different cell geometries on the same ground. The optimum cell configuration is the one that homogenises the flow without generating recirculation of the electrolyte within the cell. In that case, we can take advantage of the whole surface area of the electrodes, without the risk of gas bubbles being trapped inside the cell. In a first step, several modifications of the injection channels are considered in a reference configuration using knitted mesh-type spacers as porous transport layer (PTL). Although this indeed results in some improvement in the flow behaviour, significantly better results are obtained by the use of foams as PTL: they increase the effective cell volume covered by the electrolyte and at the same time lower the risk of flow recirculation within the cell. Furthermore, keeping the foam's pore size sufficiently large on the order of 3000 μm allows to limit the pressure drop across the cell.

1. Introduction

In the coming years, considerable efforts will have to be made to reduce greenhouse gas emissions in order to limit the increase in global average temperature to 1.5 °C, as stated by the international community through various climate agreements (Kyoto Protocol to the United Nations Framework Convention on Climate Change, 1997; Paris Agreement to the United Nations Framework Convention on Climate Change, 2015). One way to decarbonise a wide range of sectors is to use green hydrogen as an energy carrier to store and deliver usable and clean energy (Future, 2022). At present, the most sustainable way of producing hydrogen relies on the utilisation of renewable electricity, including wind and solar power or hydroelectricity, for conducting water electrolysis (Shih et al., 2022; Brauns and Turek, 2020). Currently, the two most mature technologies used to produce hydrogen are alkaline and proton exchange membrane (PEM) water electrolysis (Li, 2022). Alkaline water electrolysers (AWE) use an alkaline solution, typically KOH between 1 and 6 M, at a temperature in the range 30–80 °C, a diaphragm and Ni-based electrodes (Grigoriev et al., 2020). The primary hurdle associated with this technology revolves around improving the efficiency and diminishing capital expenditure (CAPEX) of the electrolyser (Proost, 2020). Next to this, PEM electrolysers use solid polysulfonated membranes as an electrolyte and operate at high pressure and in a range of temperatures between 20 and 80 °C (Shiva Kumar and Himabindu, 2019). The latter technology has the advantage of presenting much higher production rates but it relies on the use of costly and scarce electrocatalytic materials like Ir and Pt (Wang et al., 2022). From an economic point of view, it is highly appealing to find a way to integrate the best of these two commercially available technologies, yielding high production rates per electrode area, while benefiting from more cost-effective electrode materials.

Recent experimental studies in our group have shown that it is possible to significantly improve the performance of alkaline electrolysers by shifting from traditional gap cells to zero-gap cells, wherein the anodic and cathodic chambers are filled with 3-D porous electrodes (Rocha et al., Jun. 2022; Rocha et al., 2023). Porous nickel foams, with pore sizes ranging from 450 to 3000 μm, as well as 3-D printed triply periodic minimal surface (TPMS) geometries were studied as electrodes. The advantage of using such 3-D structures is that the available surface area for hydrogen production is much higher (Arenas et al., 2017). At the same time however, such an increased hydrogen production rate may lead to stagnant gases being trapped in the complex porous

* Corresponding author.
E-mail address: joris.proost@uclouvain.be (J. Proost).

https://doi.org/10.1016/j.ces.2025.121513
Received 12 December 2024; Received in revised form 19 February 2025; Accepted 9 March 2025
Available online 10 March 2025

channels of the electrodes. This is the reason why optimised electrolysis cells with forced electrolyte flow have been designed at the lab-scale to favour bubble removal and decrease the Ohmic resistance of the system. More specifically, the cells were designed with a double elbow at the inlet to guide the flow and enhance its spread throughout the cell, emphasising the importance of inlet effects (Weusten et al., 2021). The anodic and cathodic chambers were developed with increasing superficial area in the stream direction in order to homogenise the flow as much as possible before it enters the electrodes. This allows to take advantage of the whole area provided by the 3-D electrodes (Rocha et al., 2022). The enhanced performance of these zero-gap alkaline electrolysers has been confirmed experimentally and current densities of 2 $A{\cdot}cm^{-2}$ were observed at cell voltages lower than 2 V when using a flow-engineered laterally-graded bi-layer foam configuration (Rocha, 2024).

Up to now, such high operational current densities have barely been reached in industrial-scale alkaline electrolysers (Zhao et al., 2024; David et al., 2019) because most of them use traditional gap cells and operate under natural convection, leading to high cell voltages and high electrode coverage by gas bubbles (Jang et al., 2021). Alkaline zero-gap electrolysers with forced flow have emerged in the last years as a major development compared to traditional electrolysers (Daoudi and Bounahmidi, 2024). These systems typically use 2-D perforated/punched plates as active electrodes (Zhao et al., 2024) and porous transport layers (PTL) as elastic elements to press the electrodes onto the separator (Zhao et al., 2023). These PTL are therefore primarily meant to maintain electrical contact between the current collector plates and the electrodes. Knitted mesh or expanded mesh spacers are typically used to this end due to their simple manufacturing process (Zhao et al., 2024; Lee, 2021).

Efforts have then been made in order to apply the same methodology, i.e. moving towards zero-gap cells with knitted mesh spacers and forced electrolyte flow, to a 6-kW industrial-scale prototype electrolyser installed in our lab. Unfortunately, it was impossible to get similarly low cell voltages as with the lab-scale setup. This was attributed to the fact that the cells in our prototype electrolyser are not optimised for forced electrolyte flow, leading to a non-optimal distribution of the electrolyte in the anodic and cathodic compartments. The aim of this work is to perform Computational Fluid Dynamics (CFD) simulations to assess the behaviour of the electrolyte within one single cell in order to find some optimal configuration that simultaneously homogenises the flow and reduces recirculation of the electrolyte, thereby enhancing bubble removal. The problem of flow uniformity in electrolysis cells has already been addressed in recent literature studies (Wang et al., 2023; Xue et al., 2024; Lafmejani et al., 2018). However, it has never been tackled in combination with flow recirculation studies. Moreover, most reviews related to this topic focus on numerical modeling of hydrogen bubble generation and escape itself, using multiphase simulations (Rodríguez and Amores, 2020; Aboukalam da Cruz et al., 2023; Lee et al., 2022; El-Askary et al., 2015; Wosiak et al., 2022; Rajora and Haverkort, 2023). We believe that a first and necessary step before including electrochemistry and bubble evolution would rather be to focus on the electrolyte flow behaviour itself inside electrolysis cells, to ensure that high flow uniformity and low flow recirculation is achieved.

The main objective of this work is to define two parameters, based on single-phase flow simulations and a Residence Time Distribution (RTD) analysis, that allow to compare the performance of different cell configurations on the same ground. A first parameter will be defined to evaluate the level of flow uniformity inside the electrolysis cell, while a second one will give an estimation of flow recirculation. The aim of this parametric study is to propose a strategy to improve the distribution of flow in industrial-scale electrolysis cells. To this end, several modifications of the injection channels will first be considered in a reference configuration, using knitted mesh-type spacers as porous transport layer (PTL). Although it was found that this may indeed result in some improvement in the flow behaviour, the major novelty of this work lies in demonstrating that the use of foams as PTL has a much higher potential for both improving the flow uniformity and reducing the flow recirculation as compared to these knitted meshes that are commonly used in industry today.

2. Methodology

A dismantled view of a single cell is shown in Fig. 1(a) where the anodic and cathodic half-cells are composed of a current collector, a structural ring, a knitted mesh spacer and an electrode, and are separated by a diaphragm. The simplified geometry of the cathodic half-cell that will be considered as a reference configuration in this work is depicted in Fig. 1(b). It consists of a flat cylinder with a diameter of 20 cm and a thickness of 6 mm, filled with a knitted mesh as PTL. The electrolyte inlet is located at the bottom of the cell and has a diameter of 2 mm, while the outlet diametrically opposed at the top has a diameter of 3 mm. The electrolyte is a 30 wt% KOH solution at 70 °C with a kinematic viscosity $\nu = 8.28{\cdot}10^{-7}\ m^2{\cdot}s^{-1}$ (Le Bideau et al., 2019). Its flow is forced at the entrance of the half-cell by imposing a flow rate Q with a corresponding inlet velocity v_{in}. The inlet velocities that will be considered in this work are in the range 0.3 to 7.3 $m{\cdot}s^{-1}$, corresponding to a flow rate of 0.06 and 1.38 $l{\cdot}min^{-1}$ per cell, respectively. In order to compare our prototype cell with other cells from the industry, a new parameter is required, defined as the average velocity inside the cell:

$$v_{avg} = \frac{Q}{\varepsilon{\cdot}t_{cell}{\cdot}D_{cell,avg}} \tag{1}$$

which is the ratio between the flow rate and the average cross-section of the cell, defined as the product between the porosity inside the cell ε (which in turn depends on the 3-D structure used as PTL), the thickness of the cell t_{cell} and the average diameter of the cell $D_{cell,avg}$. The latter is obtained by integration of the cell chord length over the whole cell diameter (i.e. from $-R_{cell}$ to R_{cell}):

$$D_{cell,avg} = \int_{-R_{cell}}^{R_{cell}} \sqrt{1 - \left(\frac{y}{R_{cell}}\right)^2}\, dy = \frac{\pi{\cdot}R_{cell}}{2} \tag{2}$$

with R_{cell} the radius of the cell and y the integration variable. Based on the average velocity, it is possible to compare the prototype cell considered in this work with other industrial electrolysis cells. As an example, a comprehensive analysis of industrial scale electrolyser stacks has been reported by Sakas et al. (Sakas et al., 2022; Sakas, 2024). This study considered a 3 MW alkaline water electrolyser consisting of 2 half-stacks, each containing 163 cells connected in series, and the electrolyte flow rate was fixed to 19.9 $kg{\cdot}s^{-1}$ per half stack. Considering a 30 wt% KOH solution at 70 °C, one can calculate for each individual cell a volumetric flow rate of 6 $l{\cdot}min^{-1}$. This corresponds to an average velocity of 1.4 $cm{\cdot}s^{-1}$ if the cell thickness is fixed to 6 mm and the porosity to 98 % (which is a typical value for knitted mesh-type spacers commonly used in the industry). Considering the highest flow rate of this study, we come up with an average velocity of 2.5 $cm{\cdot}s^{-1}$ which is on the same order of magnitude as compared to industrial electrolysers. This confirms that the flow velocities considered in this work are common practice in industry as well.

In order to simulate electrolyte flow within the cell, the pimpleFoam solver implemented in OpenFOAM was used to solve the incompressible Navier-Stokes equations for single-phase flow, based on the finite volume method (Batchelor, 1967):

$$\nabla \bullet \boldsymbol{u} = 0 \tag{3}$$

$$\frac{\partial \boldsymbol{u}}{\partial t} + (\boldsymbol{u} \bullet \nabla)\boldsymbol{u} = -\frac{1}{\rho}\nabla p + \nu\nabla^2\boldsymbol{u} + \boldsymbol{g} \tag{4}$$

where $\boldsymbol{u}$ (u, v) is the velocity field, ρ the density of the fluid, p the pressure and $\boldsymbol{g}$ accounts for gravity. The boundary conditions for the

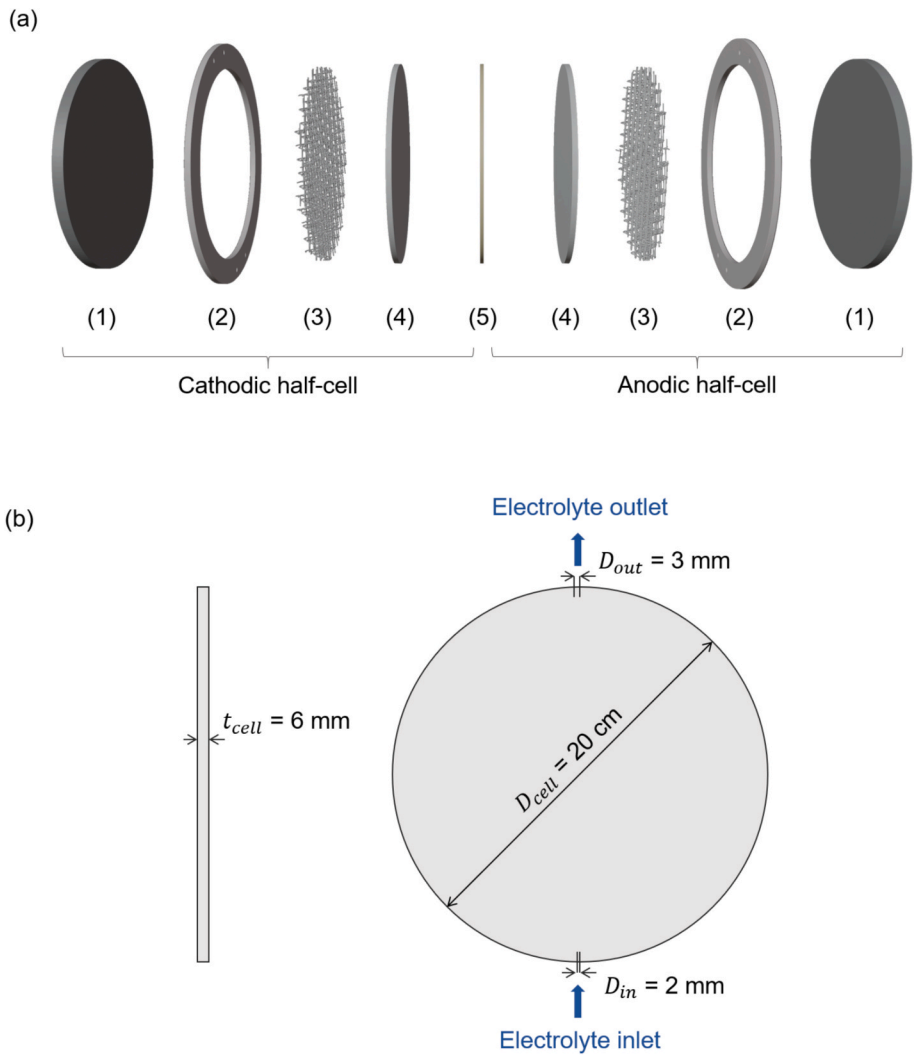

Fig. 1. (a) Dismantled industrial scale prototype cell with (1) current collector plate, (2) structural ring, (3) knitted mesh spacer, (4) electrode and (5) separator; (b) Simplified representation of the cathodic half-cell used as a reference configuration for the simulations from side (left) and front (right) view. The knitted mesh filling the half-cell is modelled by implementing a Darcy-Forchheimer drag force in OpenFOAM.

simulation are the inlet velocity v_{in}, the pressure at the outlet, which is fixed to 0 $m^2 \cdot s^{-2}$ without loss of generality, and the no-slip condition at the lateral walls. The assumption of 2-D flow is made since a plug flow develops across the thickness of the half-cell in the turbulent regime. Due to the small inlet diameter D_{in} of the cell and to the imposed electrolyte flow rate, a jet flow is expected to develop within the cell and the corresponding Reynolds number can be calculated as (Lee et al., 2003):

$$\mathrm{Re} = \frac{v_{in} \cdot D_{in}}{\nu} \tag{5}$$

Since jet flow fields are likely to exhibit laminar properties at Re < 1000 (Zuckerman et al., 2006), a laminar model[1] is used for inlet velocities lower than 0.4 $m \cdot s^{-1}$ and the k-ω turbulent model available in OpenFOAM is used to account for turbulence at higher flow rates. The turbulent boundary conditions at the inlet are specified as follows:

$$k = \frac{3}{2} \cdot (I \cdot v_{in})^2 \tag{6}$$

$$\omega = \frac{k^{0.5}}{C_{\mu}^{0.25} \cdot l} \tag{7}$$

with k the turbulent kinetic energy, I the turbulence intensity which is fixed to 0.05, ω the turbulence specific dissipation rate, C_{μ} a model constant equal to 0.09 and l a reference length scale (fixed to $0.01 \cdot D_{cell}$). The end time of the simulations $t_{f,1}$ is fixed based on the inlet velocity magnitude to ensure a stationary solution is reached in each case. The time step size Δt is fixed to 0.001 s.

Concerning the integration of porous media as PTL within the cell, it is in principle possible to explicitly include the exact PTL geometry, i.e. based on high-resolution micro-CT (computed tomography) scanned data (Kuhlmann et al., 2022; Sadeghi et al., 2020) into the simulations. Unfortunately, this is highly demanding from a computational point of view. To counter this problem, spatially averaged equations have been used to implicitly account for porosity based on the Darcy-Forchheimer law (Edouard et al., 2008):

$$\left|\frac{\Delta p}{L}\right| = \frac{1}{k_1} \cdot \mu \cdot v + k_2 \cdot \rho \cdot v^2 \tag{8}$$

[1] For the laminar flow regime, the plug flow assumption does not hold. So, for the 2-D assumption to be valid in this regime, one would have to account for the viscous dissipation in the cross-stream direction through a Darcy's like term. However, we have omitted this contribution as the empty cell is not the main focus of this work.

with $|\Delta p/L|$ the pressure drop per unit length, μ the dynamic viscosity of the fluid, k_1 the Darcian permeability and k_2 the non-Darcian coefficient of the porous structure. In what follows, the Darcian permeabilities and non-Darcian coefficients of a knitted mesh spacer and of one of the foams previously used in our experimental studies (Rocha et al., 2022) will first be extracted in order to implicitly account for these structures in the simulations.

Pressure drop calculations using the pimpleFoam solver were performed numerically on a $10 \times 10 \times 0.9$ cm^3 industrial knitted mesh-type spacer having a porosity $\varepsilon = 0.98$. Based on a CAD model provided by an industrial partner, the knitted mesh was reconstructed in OpenFOAM thanks to the snappyHexMesh utility. The geometric details of the knitted mesh are shown in Fig. 2. As illustrated in Fig. 3, the calculated data were then fit with the Darcy-Forchheimer eq. (8) to extract the Darcian permeability k_1 and the non-Darcian coefficient k_2 of the knitted mesh. The following values were obtained: $k_1 = (1.26 \pm 0.01)\cdot10^{-5}$ m^2 and $k_2 = 10.29 \pm 0.13$ m^{-1}. Next to this, a foam specimen was also considered, having a pore size of 3000 μm and presenting a porosity of 0.94 (Rocha et al., 2022). $|\Delta p/L|$ calculations were performed based on micro-CT scans of a $2 \times 2 \times 0.56$ cm^3 foam sample, using the same methodology as explained in (Rocha, 2024) to reconstruct the foam from the scans. This resulted in the following parameters: $k_1 = (94.76 \pm 5.35)\cdot10^{-9}$ m^2 and $k_2 = 290.46 \pm 0.61$ m^{-1}. As shown in Fig. 3, the pressure drop calculations of the 3000 μm pore-sized foam showed good agreement with a similar foam from the literature (Liu et al., 2006).

It can already be observed from Fig. 3 that the 3000 μm foam exerts a significantly larger influence on the flow than the knitted mesh-type PTL, resulting in a substantial increase in pressure drop: 3.6 bar·m^{-1} at 1 m·s^{-1} for the 3000 μm foam as compared to 0.1 bar·m^{-1} for the knitted mesh. As the respective porosities already suggested, the foam is much denser than the knitted mesh, which explains the larger pressure difference generated as liquid flows through it. This already emphasises the fact that foams will be more suited to guide the electrolyte flow, contrarily to knitted meshes whose primary function is rather to maintain some space between the gas separator and the current collector plates while still guaranteeing electrical contact.

In order to assess flow uniformity and flow recirculation within the electrolysis cell, two parameters have been defined based on a Residence Time Distribution (RTD) analysis. This method consists of injecting tracers at the inlet of the cell at time $t = 0$ s and then measuring the concentration of tracers at the outlet as a function of time $C_{out}(t)$. This concentration can be determined numerically by solving the convection–diffusion equation for the concentration field $C(x,y,t)$ (Probstein, 2005):

$$\frac{\partial C}{\partial t} + \boldsymbol{u} \bullet \nabla C = D\nabla^2 C \tag{9}$$

where D is the diffusivity of the tracers within the fluid considered. In our simulations, a diffusivity value of $5\cdot10^{-9}$ m^2·s^{-1} was taken, corresponding to the diffusivity of hydrogen in a 30 wt% KOH solution at 70 °C (Tham et al., 1970). The scalarTransportFoam solver of OpenFOAM has been used to calculate C based on a step injection of the

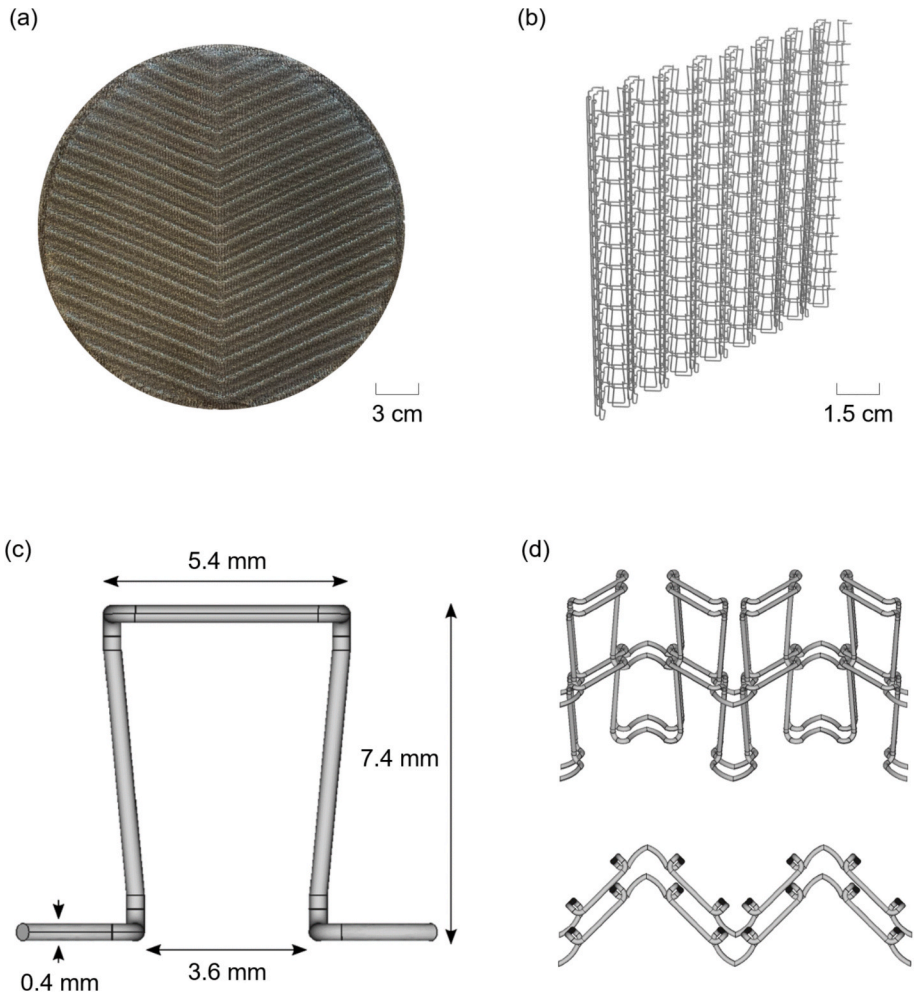

Fig. 2. (a) Optical micrograph of a knitted mesh-type spacer commonly used as PTL in industrial electrolysers; (b) CAD model for the knitted mesh used as PTL in the current study; (c) Geometric details of one basic element; (d) Front and upper view of the knitted mesh-type spacer.

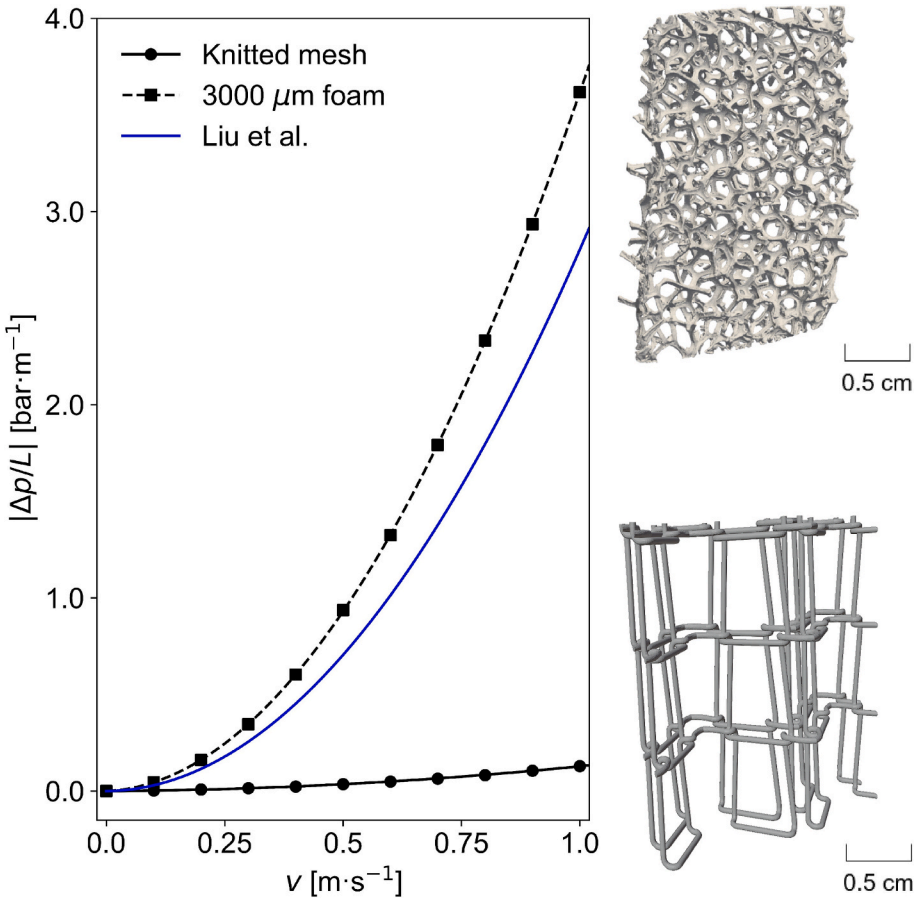

Fig. 3. Evolution of the pressure drop per unit length $|\Delta p/L|$ as a function of upstream velocity v considering a 30 wt% KOH solution at 70 °C for an industrial knitted mesh and a 3000 μm foam. (Blue curve) Comparison with experimental data from the literature (Liu et al., Mar. 2006). (For interpretation of the references to colour in this figure legend, the reader is referred to the web version of this article.)

tracers (Li, 2017) at the inlet, with impermeable boundary conditions at the wall, and an open boundary at the outlet. This solver uses the velocity field computed at $t_{f,1}$ in the single-phase simulations to calculate the scalar transportation, meaning that $\boldsymbol{u}$ is considered to be stationary in eq. (9). The end time of this step injection is set to $t_{f,2} = 180$ s to make sure that $C_{\text{out}}(t)$ becomes constant and equal to the concentration of the feed. Based on this concentration profile, it is possible to calculate the cumulative distribution function and the RTD function $E(t) = \frac{C_{\text{out}}(t)}{\int_0^{t_{f,2}} C_{\text{out}}(t)\,\mathrm{d}t}$, the latter giving an indication of the number of fluid elements leaving the cell after having spent a given time.

The first parameter, aimed at determining flow uniformity and the presence of dead/stagnant zones within the cell, is the dimensionless time θ (Wang et al., 2023). It is defined as the ratio between the mean residence time of the fluid inside the cell of volume V and the space time, i.e. the time that would be required to fill the whole space available at a fixed inlet flow rate Q:

$$\theta = \frac{t_m}{\tau} = \frac{\int_0^{t_{f,2}} t \cdot E(t)dt}{V/Q} \tag{10}$$

This parameter gives an image of the effective volume used inside the cell. Two cases can be identified: $\theta < 1$ and $\theta \geq 1$. If $\theta < 1$, this means that $t_m < \tau$ and hence that the mean time spent by the fluid inside the cell is lower than the time required to fill it. In other words, there will be some dead/stagnant zones of low velocity in the cell where no gas will be produced. On the other hand, when $\theta \geq 1$, $t_m \geq \tau$ which means that fluid elements remain in the cell for a time higher or equal to the space time. In this case, the electrolyte will have time to homogenise over the whole cell volume and to fill its entire space. As a result, no dead zones are to be expected and the electrolyte will be uniformly distributed over the entire electrode area, enhancing hydrogen production. Note that when porous media are added inside the cell, the porosity of these 3-D structures must be considered in the computation of the space time τ, so that $\tau = \varepsilon \cdot V/Q$. In other words, the volume of the cell available for the electrolyte will be smaller when it is filled with a porous transport layer, leading to slightly lower space times.

Another phenomenon which may occur during hydrogen production inside the electrolysis cell is the entrapment of hydrogen bubbles inside the domain. For this reason, it is interesting to determine whether the electrolyte goes directly from the inlet to the outlet of the half-cell or if it recirculates, the latter leading to a poor evacuation of the bubbles. A second parameter is therefore defined to characterise this recirculation phenomenon, namely the dimensionless variance σ_θ^2 (Nauman, 2003). It is defined as the ratio between the variance of the RTD function and the square of the mean residence time:

$$\sigma_\theta^2 = \frac{\sigma^2}{t_m^2} = \frac{\int_0^{t_{f,2}} (t - t_m)^2 \cdot E(t)dt}{\left(\int_0^{t_{f,2}} t \cdot E(t)dt\right)^2} \tag{11}$$

When $\sigma_\theta^2 = 0$, this means that there is no recirculation of the flow since the RTD function presents no dispersion around the mean residence time. This case corresponds to an ideal plug flow (Nauman, 2003). On the other hand, when $\sigma_\theta^2 > 0$, some recirculation of the flow occurs, which could lead to entrapment of hydrogen bubbles in the cell.

In order to simulate multiphase flow within the cell, a mixture model formulation (Ishii and Hibiki, 2011) has been used and implemented on

the driftFluxFoam solver available in OpenFOAM. This solver solves the continuity and momentum eq. (3) and (4) for a gas–liquid mixture by weight-averaging velocity, density and viscosity as a function of the gas fraction α. In the simulations, the gas fraction at the inlet of the cell α_{in} was imposed as an additional boundary condition compared to single-phase simulations. The density of the gas was set to 0.08 kg·m^{-3} and the dynamic viscosity to $0.88 \cdot 10^{-5}$ Pa·s (Rocha, 2024).

Finally, the meshing strategy that was used to discretise the computational domain into hexahedral elements is represented in Fig. 4. The mesh was generated with the blockMesh utility offered by OpenFOAM. Fig. 4(a) shows the computational mesh developed for the cathodic half-cell, consisting of 6000 elements and 11 blocks. Dividing the space into several blocks allows to keep all meshing elements hexahedral and to avoid the presence of irregular cells. As observed in Fig. 4 (a), the three cells sharing the red point as vertex have a regular shape. Moreover, a grading of the elements was applied in order to refine the zones close to the inlet and the outlet of the domain, as these are well-known critical locations in terms of flow distribution and evacuation (Rocha et al., 2022; Weusten et al., 2021). A mesh sensitivity analysis was then performed by computing the pressure drop per unit length $|\Delta p/L|$ between the inlet and the outlet of the cell as a function of the number of meshing elements, considering an inlet velocity of 1.5 m·s^{-1}. As observed in Fig. 4(b), the pressure drop tends towards a constant value as the mesh gets finer, meaning that the mesh does not influence the results anymore. As it can be seen in Fig. 4(c), the related computational times (CPU times) were also calculated, logically showing an increasing trend as the number of elements rises. We observe that at least 12 h of computation time (running the simulation in parallel and using 4 cores on the supercomputing facilities of our university) are required when the mesh is made of 300,000 elements or more. For this reason, and since Δp starts to stabilise in this region, a reference mesh of 230,000 elements has been chosen for all simulations.

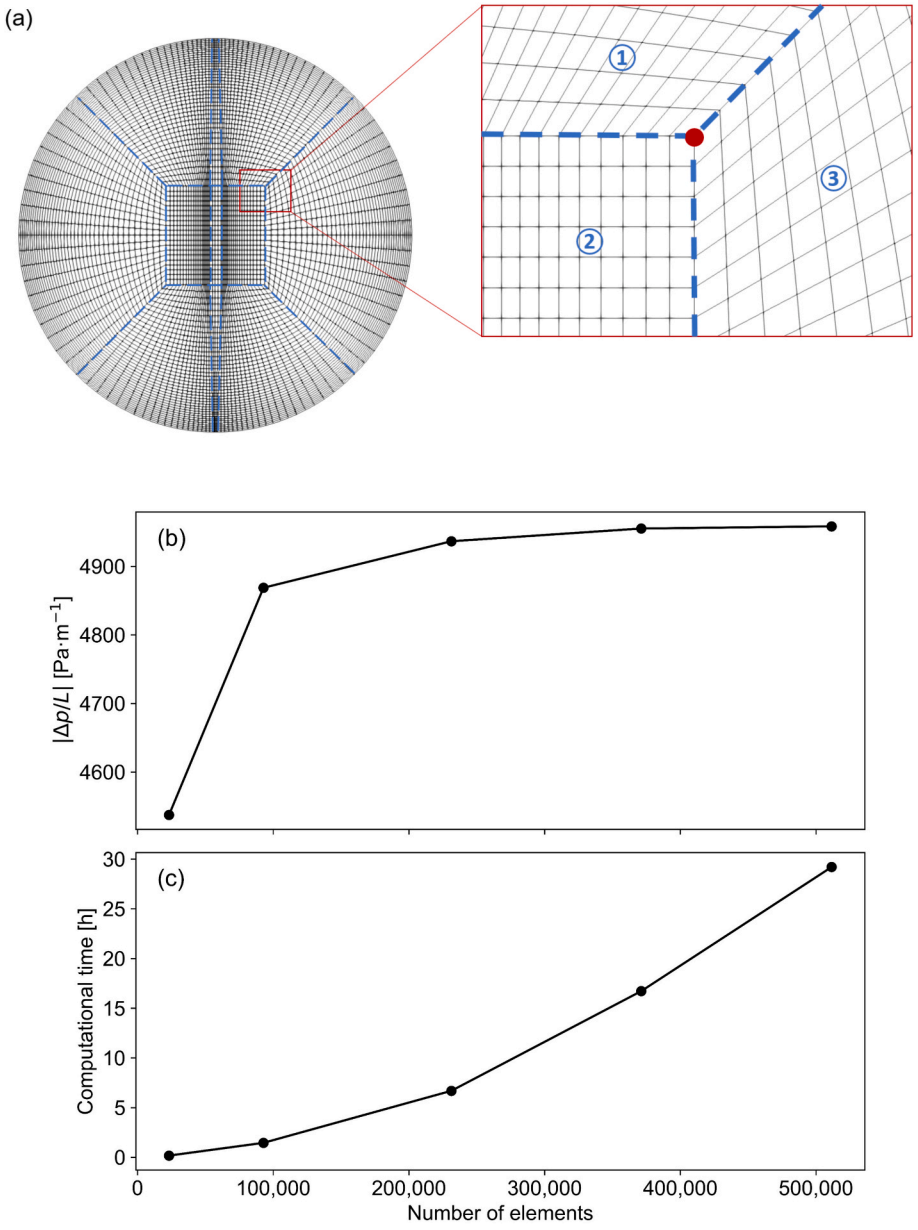

Fig. 4. (a) Computational mesh made of 11 blocks and 6000 elements with the intersection (red point) between three blocks (denoted 1, 2 and 3) being highlighted; (b) Evolution of the pressure drop per unit length $|\Delta p/L|$ and of (c) the computational time (CPU time) as a function of the number of meshing elements for $v_{in} = 1.5$ m·s^{-1}. (For interpretation of the references to colour in this figure legend, the reader is referred to the web version of this article.)

3. Results and discussion

The parametric study described in the previous section was first applied to the reference cell configuration already shown in Fig. 1(b) with a knitted mesh-type spacer. Fig. 5(a) shows a typical velocity profile inside the domain for an inlet velocity of 1.5 m·s^{-1}. As expected, the electrolyte forms a jet stream at the entrance of the half-cell due to the small inlet diameter compared to the much larger diameter of the cell chamber. This leads to an inhomogeneous distribution of the flow, with some zones that are not flushed by the electrolyte (dead zones) and some recirculation near the outlet (diametrically opposed at the top). As can be observed in Fig. 5(b), this jet stream behaviour is also confirmed by the KOH deposits that we collected on one of our prototype's current collector plates after a series of tests.

Computation of the dimensionless time θ then allows to quantify the degree of homogeneity. Its profile as a function of inlet velocity v_{in} (bottom axis) and corresponding average velocity v_{avg} (top axis) is shown in Fig. 5(c). It clearly shows that flow uniformity increases as the inlet flow rate increases, as expected. However, for the range of velocities considered, the dimensionless time remains quite low (lower than 0.6) meaning that distribution of the electrolyte is still rather poor. In order to quantify the occurrence of recirculation of the flow, the dimensionless variance is shown in Fig. 5(d). It appears that σ_θ^2 also increases with increasing inlet velocity, which means that a higher flow rate also leads to more recirculation. This explains why there are fewer dead zones when the inlet flow rate is increased. Contradictory conclusions arise from these two parameters, since a higher flow rate is desired from a uniformity point of view, while lower velocities will

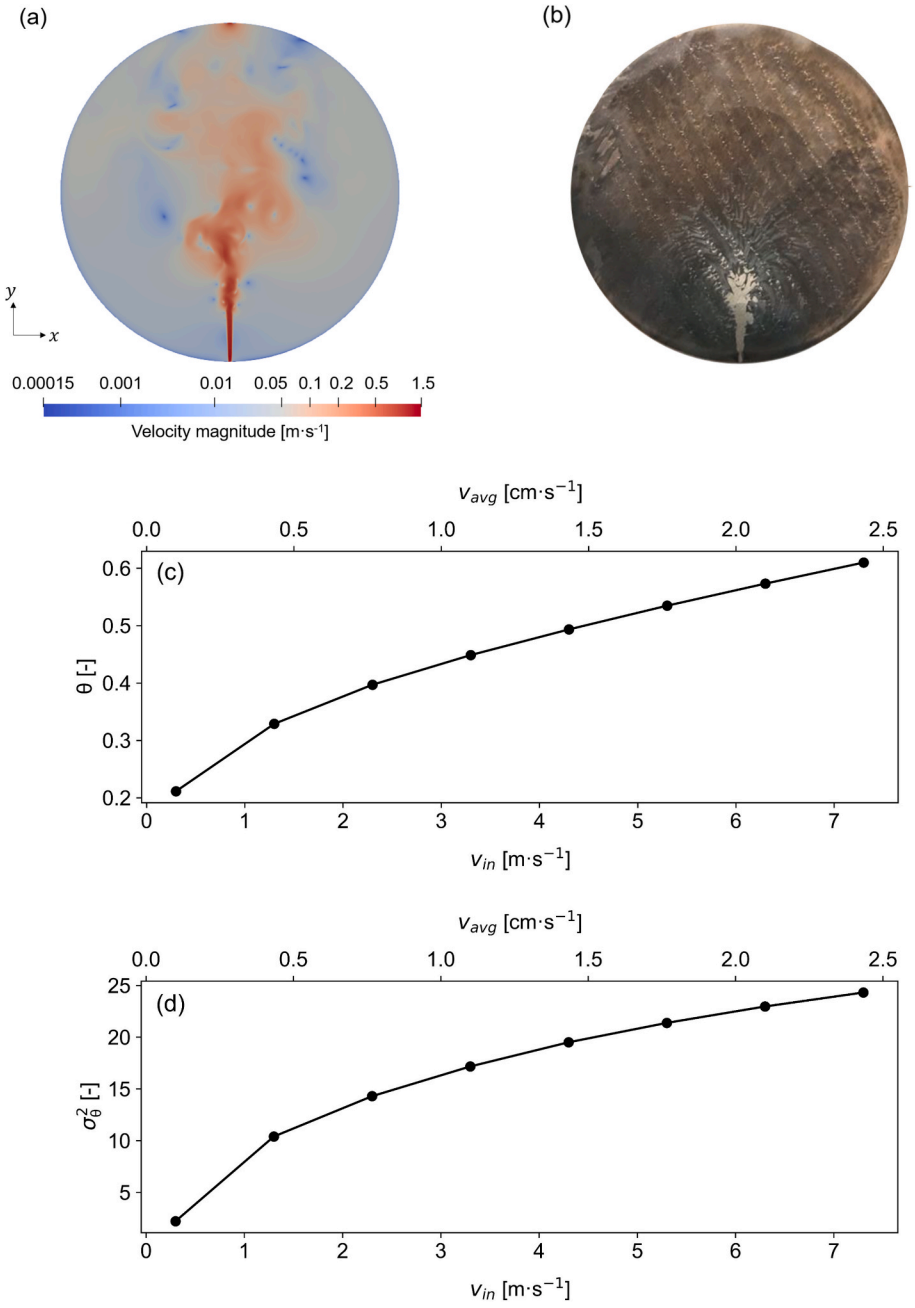

Fig. 5. (a) Velocity profile at time t = 5 s (in log-scale and with laminar model) for the reference cell with the knitted mesh and v_{in} = 1.5 m·s^{-1}; (b) KOH deposits observed on a current collector plate in our prototype electrolyser; (c) Dimensionless time θ and (d) dimensionless variance σ_θ^2 as a function of inlet velocity v_{in} (bottom axis) and average velocity v_{avg} (top axis).

generate less recirculation of the flow. Since the dimensionless time remains very low and the dimensionless variance relatively high (far above 1), new configurations need to be considered in order to improve the performance of the electrolyser.

At first, since the inlet opening seems to be a crucial point in terms of flow distribution, some modifications were applied to the reference configuration and two different inlet configurations have been studied: an inclined inlet (at 45° to the right) and three inlets. Note that for each configuration studied, the volumetric flow rate was kept constant and the corresponding inlet velocity was calculated accordingly. A video comparing the velocity profiles of these three configurations is available in the Supplementary Information section. The dimensionless times and variances of these two new configurations have been compared to the reference case in Fig. 6. Concerning flow uniformity, it appears from Fig. 6(a) that inclining the inlet channel or increasing the number of inlets clearly lowers the risk of dead zones in the cell. Indeed, dimensionless times close to unity are reached for high inlet velocities when more than one inlet is envisaged. Next to this, Fig. 6(b) highlights the fact that the cell with an inclined inlet is more suited to avoid recirculation of the flow as compared to the reference configuration because the electrolyte is now directly guided towards the outlet. As it was already the case for flow uniformity, the use of multiple inlets is even more interesting since lower values of σ_θ^2 can be reached. Another relevant observation is that the dimensionless variance globally increases with v_{in} for all these cases. This clearly highlights the fact that simply increasing the flow rate inside the cell is not the best option since there will be a price to pay in terms of flow recirculation, even if the flow is better distributed.

From these observations, the case with three inlets might seem the most suited to improve the flow distribution while simultaneously also lowering the level of recirculation. However, this configuration is not necessarily the best from an operational point of view due to the high discrepancy between both dimensionless parameters at low and high inlet velocities. For instance, if the number of cells in the electrolyser increases, the inlet flow rate in one cell will be lower for a constant volumetric pumping rate. This then implies that the value of θ will

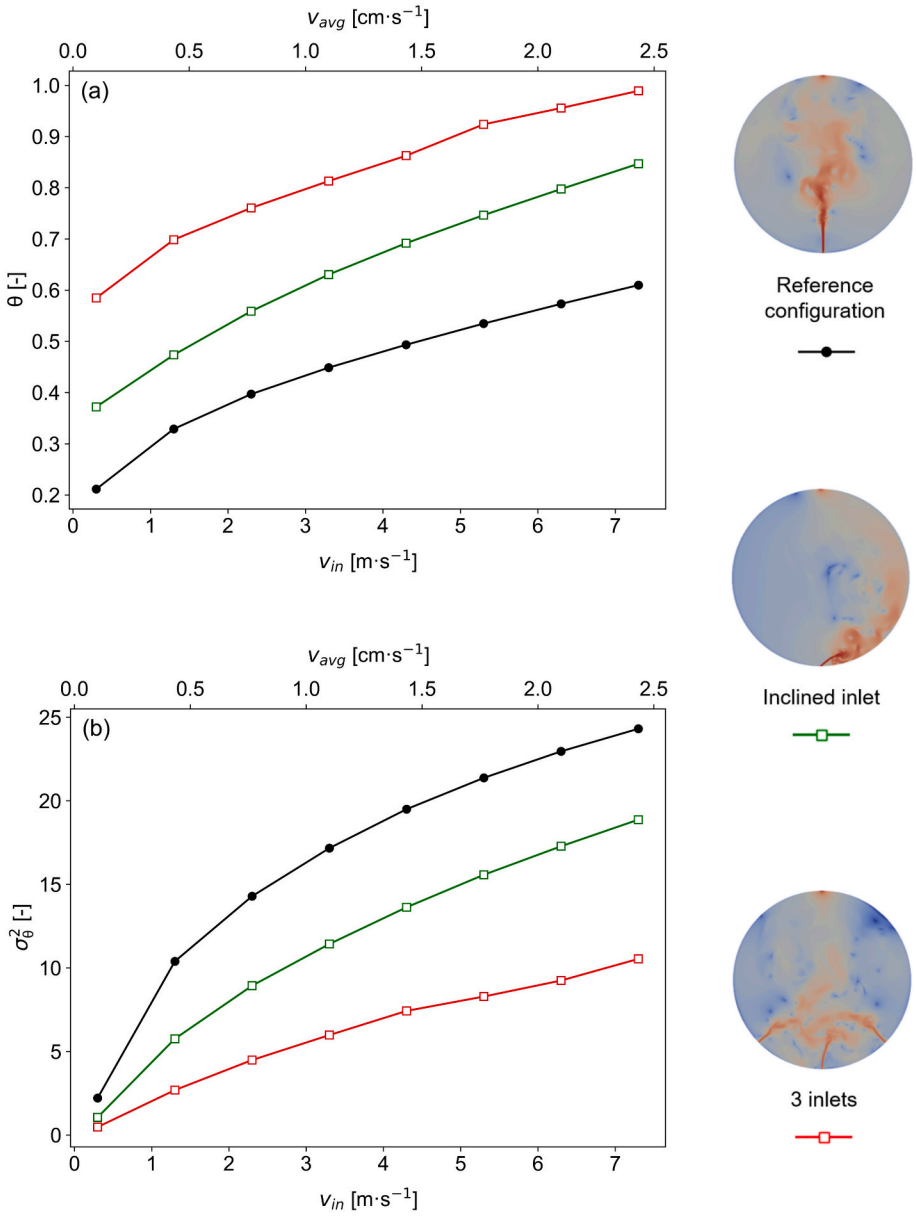

Fig. 6. (a) Dimensionless time θ and (b) dimensionless variance σ_θ^2 as a function of inlet velocity v_{in} (bottom axis) and average velocity v_{avg} (top axis) for different inlet configurations, all using a knitted mesh-type spacer as PTL.

decrease significantly, generating more dead zones in the cells. The same remark holds for the dimensionless variance when decreasing the number of cells: it will then increase significantly when moving towards higher inlet velocities, leading to more recirculation. In other words, we should also aim to identify a configuration characterised by dimensionless parameters that exhibit minimal sensitivity to changes in v_{in}.

To tackle this challenge, we considered the substitution of the conventional knitted mesh-type porous transport layers by foams. Fig. 7 compares the values of θ and σ_θ^2 for the reference configuration, the case with three inlets (both using a knitted mesh) and for a cell using a 3000 μm foam as PTL. Fig. 7(a) points out the net improvement that foams can create in terms of flow uniformity. Due to the intricated channels of the foam, the electrolyte is likely to travel through some preferential pore paths, while at the same time experiencing a significant drag force from the structure. This leads to high residence times and a value of θ higher than 1. In other words, no dead zones are expected, contrarily to the reference configuration and the case with 3 inlets. This also highlights the fact that the knitted mesh-type spacers typically used in industry today do not help at all to homogenise the flow inside the cell. On top of that, Fig. 7(b) shows that the use of foams also significantly lowers the value of σ_θ^2 (even approaching 0), meaning that no recirculation is to be expected. This clearly underlines the interest of using foams as porous transport layers in water electrolysers: they naturally improve uniformity of the flow while simultaneously avoiding electrolyte recirculation. At the same time, they are also less sensitive to changes in the inlet velocity. Note that in contrast to the previous figures where the average velocity was plotted on the top axis, the flow rate Q is now shown on the secondary axis of Fig. 7, as the average velocity is not suitable for comparing different PTL types due to its dependence on porosity (see eq. (1)). As an illustration, another video available in the Supplementary Information section compares the velocity profiles of an empty cell (i.e. without any PTL), the reference configuration (using a knitted mesh-type spacer as PTL) and the cell filled with a 3000 μm foam.

These two aforementioned phenomena are explicitly confirmed by the velocity vectors shown in Fig. 8 for the reference configuration with a knitted mesh (a, left) and the case where the cell is filled with a 3000

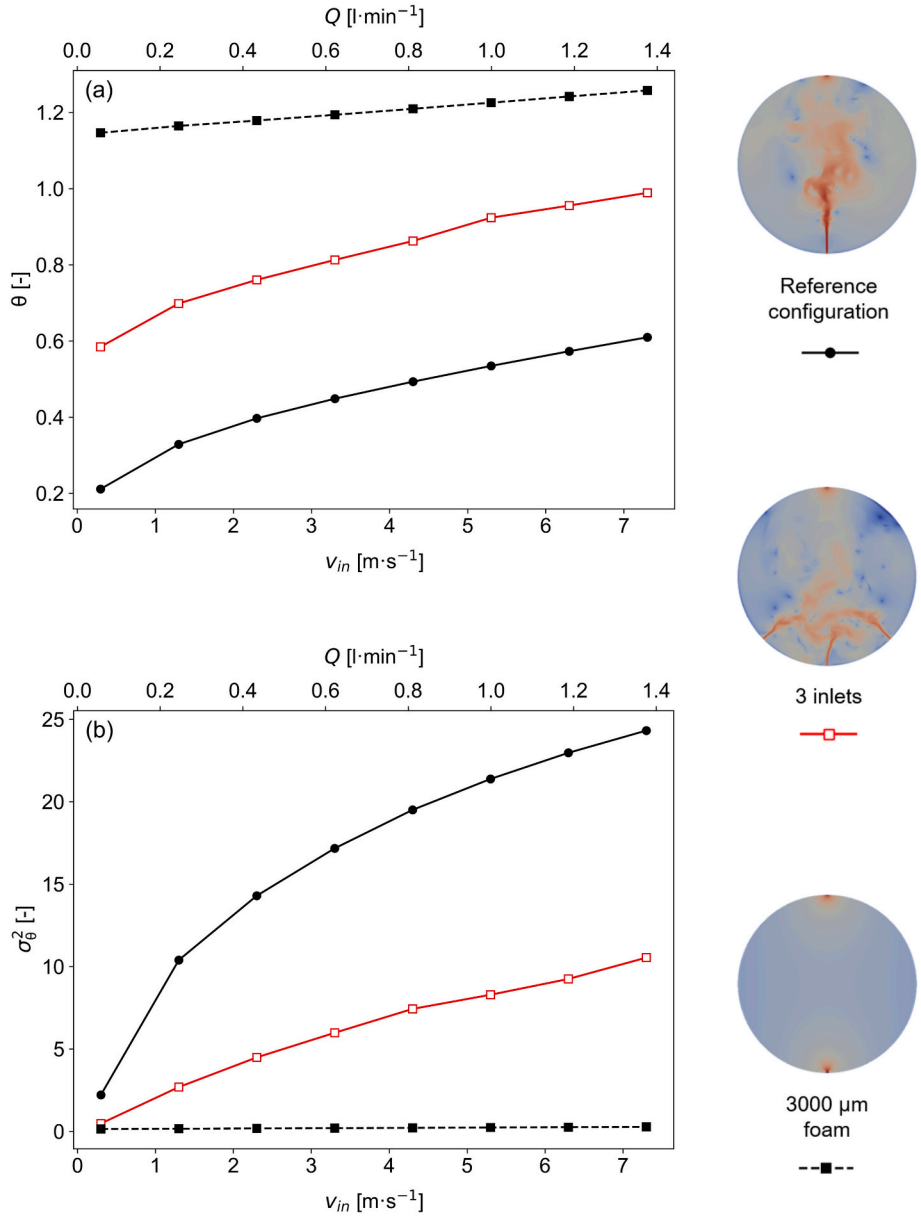

Fig. 7. (a) Dimensionless time θ and (b) dimensionless variance σ_θ^2 as a function of inlet velocity v_{in} (bottom axis) and flow rate Q (top axis), comparing a knitted mesh and a 3000 μm foam as PTL.

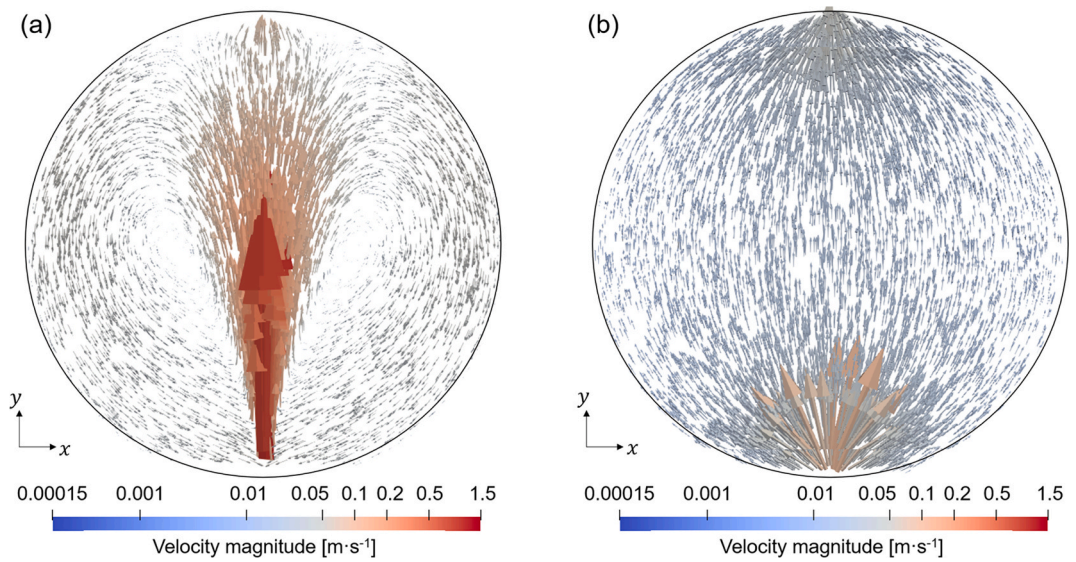

Fig. 8. Velocity vectors coloured by magnitude (in log-scale) at an inlet velocity $v_{in} = 1.5$ m·s^{-1} for (a) the reference cell with a knitted mesh and (b) using a 3000 μm foam as PTL.

μm foam (b, right). In the first case, some electrolyte is clearly recirculating on the borders of the cell and the zones next to the central jet stream present zero velocities. This is completely different in the configuration with the 3000 μm foam where all velocity vectors point in the same (upward) direction and no dead zones are observed. This is fully in line with the observation in Fig. 7 of a dimensionless time close to 1 and a dimensionless variance close to 0. The main hurdle related to the use of foams as PTL is that the electrolyte velocity, although being homogeneously distributed, will be much lower inside the cell. In other words, even if gas could potentially be produced everywhere in the half-cell, efforts are still required to ensure that the electrolyte velocity is still sufficiently high for an efficient gas removal.

To this end, some preliminary multiphase simulations have been performed on the same cell geometry, considering an inlet velocity of 1.5 m·s^{-1}. In order to determine if the gas is correctly brought to the outlet, a mixture 50 % electrolyte – 50 % gas is injected inside the cell (i.e. the gas fraction at the inlet α_{in} is fixed to 0.5) and the gas fraction at the outlet α_{out} is calculated numerically as a function of time. The results are shown in Fig. 9 for three distinct cases: the reference cell configuration with a knitted mesh-type spacer, the cell filled with a 3000 μm foam and an empty cell. Two important conclusions can be extracted from this graph. First of all, we see that the gas fraction at the outlet of the cell takes more time to start increasing when it is filled with a foam. This is indicative for the obstruction caused by the foam and for the fact that the flow will be more homogeneously distributed throughout the cell before reaching the outlet. In the two other cases, some gas reaches the outlet more rapidly due to the jet stream behaviour, but will take more time to tend towards its final value (i.e. $\alpha_{out} = 0.5$). In other words, this gives an indication of the flow uniformity and of the presence of dead zones in the cell. Moreover, it also shows that efficient gas removal

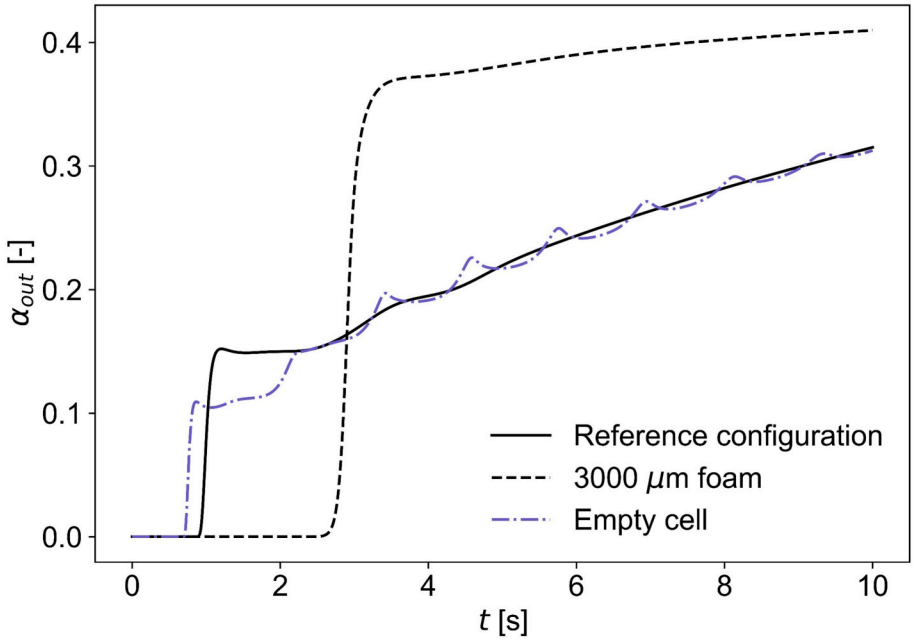

Fig. 9. Gas fraction at the outlet of the cell α_{out} as a function of time t with $\alpha_{in} = 0.5$ and $v_{in} = 1.5$ m·s^{-1}, comparing an empty cell configuration with the use of a knitted mesh and a 3000 μm foam as PTL.

can be achieved even when the flow velocities are low (i.e. when the 3000 μm foam is used as PTL). A second observation is related to the reference cell (and this behaviour is even more pronounced when the cell is empty). When looking at the related curves, we see that after reaching a first plateau, the gas fraction presents some peaks and oscillates while keeping increasing. This is due to some recirculation of the mixture as it approaches the outlet. It then goes back towards the interior of the cell along its borders before facing the central jet and being transported back to the outlet, generating a new peak on the graph. This behaviour disappears with time as less recirculation is observed. These oscillations are not observed when the 3000 μm foam is used as PTL, meaning that no recirculation effects are to be expected. These results are totally in line with the analysis that was made previously (see Figs. 7 and 8), which demonstrates the interest of defining the dimensionless parameters θ and σ_θ^2 based on single-phase simulations.

The low flow velocities when using foam-based PTL are mainly due to the high pressure drop generated by the foam structure that comes at the expense of an improved flow homogenisation and a reduced flow recirculation. As observed in Fig. 10(a), additional pressure drop calculations were also performed on a foam having a smaller pore size of only 450 μm and presenting a porosity of 0.85 (Rocha et al., 2022). The same methodology as described previously based on micro-CT scans was used to extract the parameters $k_1 = (2.62 \pm 0.13)\cdot10^{-9}$ m^2 and $k_2 = 2437.31 \pm 2.58$ m^{-1} for the 450 μm foam. As compared to the other 3-D structures studied in this work, the influence on the flow is even larger in this case in terms of pressure drop, with 33 bar·m^{-1} calculated at 1 m·s^{-1}. It is worth noticing that the fit shows once more good agreement with a similar foam from the literature (Innocentini et al., 1999). Fig. 10 (b) compares the pressure drop per unit length $|\Delta p/L|$ as a function of inlet velocity v_{in} for the two cases shown in Fig. 8, as well as for a cell filled with a 450 μm foam. Note that this graph fundamentally differs from the results presented in Figs. 3 and 10(a), which focused on isolated 3-D structures (i.e. not yet incorporated into the cell geometry), thereby assuming a uniform upstream velocity v flowing through the knitted mesh or foam. In this case, the inlet velocity within the cell becomes the variable of interest, and the associated pressure drop is affected by the specific geometry of the cell. Once again, the corresponding flow rate is indicated on the graph. It can be observed that the addition of foams within the cell leads to higher pressure drops compared to the use of traditional spacers. This means that there will be a price to pay in terms of pumping power when such foams are used as alternative PTL. However, even for the highest inlet velocity and considering a cell diameter of $L = 1$ m, the pressure gradient generated by the 3000 μm foam remains smaller than 2 bar. This is negligible with respect to typical operating pressures of 30 bar. On the contrary, the 450 μm foam would lead to a pressure drop on the order of 12 bar, which is much more significant. This highlights the necessity for maintaining the foam's pore size above a specific threshold to ensure that the foam structure still exhibits sufficiently open channels for facilitating electrolyte flow. In any case, simply modifying the geometry of the PTL (i.e. replacing knitted mesh-type spacers by foams) remains much easier than changing the entire cell design.

As a summary, the different inlet configurations presented in Fig. 6 (i.e. 1 inlet, inclined inlet and 3 inlets) have been compared in Table 1 in terms of flow uniformity (θ), flow recirculation (σ_θ^2) and pressure drop per unit length ($|\Delta p/L|$ in bar.·m^{-1}), for an inlet velocity of 1.3 m.·s^{-1}. The three types of porous transport layers studied in this paper (i.e. knitted mesh-type spacer, 3000 μm foam and 450 μm foam) have been considered in each case. From this table, the configuration with 1 inlet and the 3000 μm foam used as PTL clearly stands out as it strongly homogenises the flow ($\theta \geq 1$), reduces recirculation ($\sigma_\theta^2 \to 0$) and maintains the pressure drop on a reasonable range, while not modifying the entire cell design.

4. Conclusions

In this work, single-phase CFD simulations have been used to extract, based on a Residence Time Distribution (RTD) analysis, two representative parameters (θ and σ_θ^2) that allow to quantify electrolyte flow

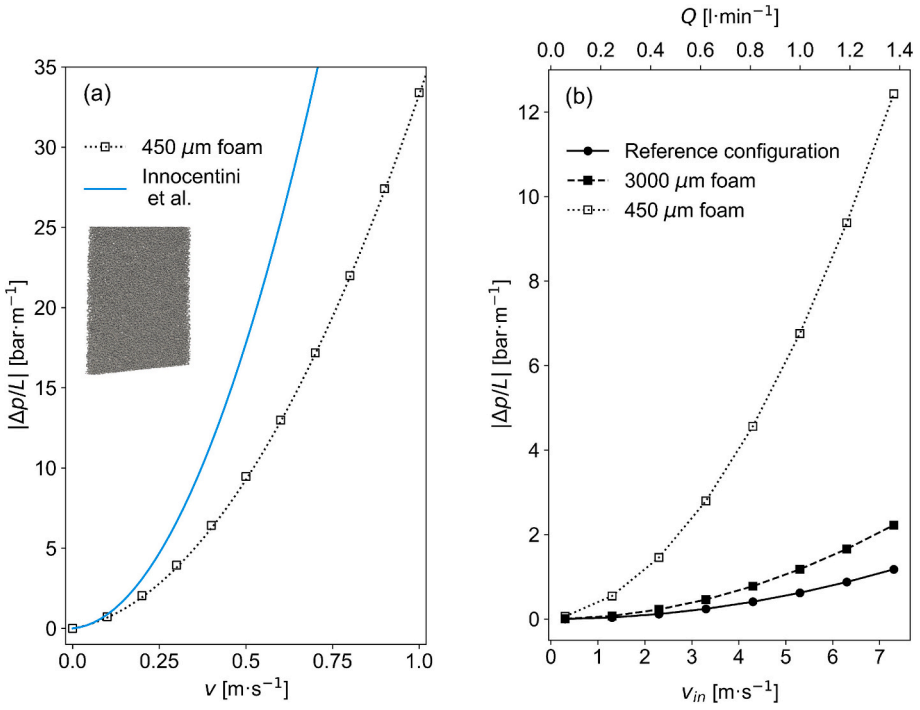

Fig. 10. (a) Evolution of the pressure drop per unit length $|\Delta p/L|$ as a function of upstream velocity v for a 450 μm foam considering a 30 wt% KOH solution at 70 °C. (Blue curve) Comparison with experimental data from the literature (Innocentini et al., Oct. 1999). (b) Evolution of the pressure drop per unit length $|\Delta p/L|$ as a function of inlet velocity v_{in} (bottom axis) and flow rate Q (top axis), comparing the reference cell configuration with a knitted mesh to the use of both a 3000 μm and 450 μm foam as PTL. (For interpretation of the references to colour in this figure legend, the reader is referred to the web version of this article.)

Table 1
Comparison between different inlet configurations in terms of flow uniformity (θ), flow recirculation (σ_θ^2) and pressure drop per unit length ($|\Delta p/L|$, expressed in bar·m^{-1}), for different types of PTL and with $v_{in} = 1.3$ m·s^{-1}.

	1 inlet			Inclined inlet			3 inlets		
	θ	σ_θ^2	$\lvert\Delta p/L\rvert$	θ	σ_θ^2	$\lvert\Delta p/L\rvert$	θ	σ_θ^2	$\lvert\Delta p/L\rvert$
Knitted mesh	0.33	10.40	0.04	0.47	5.76	0.02	0.70	2.69	0.04
3000 μm foam	1.16	0.17	0.07	1.64	0.18	0.04	1.14	0.07	0.06
450 μm foam	1.20	0.15	0.55	1.68	0.15	0.32	1.25	0.06	0.33

uniformity and flow recirculation in water electrolysis cells, and hence to compare different cell geometries on the same ground. The optimum cell configuration is the one that homogenises the flow ($\theta \geq 1$) without generating recirculation of the electrolyte in the cell ($\sigma_\theta^2 \to 0$). In that case, we can take advantage of the whole surface area of the electrodes, without the risk of gas bubbles being trapped inside the cell. In a first step, several modifications of the injection channels have been considered in a reference configuration using knitted mesh-type spacers as porous transport layer (PTL). Although it was found that this may indeed result in some minor improvement in the flow behaviour, significantly better results are obtained by the use of foams as PTL: they increase the effective volume covered by the electrolyte and at the same time lower the risk of flow recirculation within the cell. Furthermore, keeping the foam's pore size sufficiently large (on the order of 3000 μm) allows to limit the increase in pressure drop and hence the need for a higher pumping power.

CRediT authorship contribution statement

Kevin Van Droogenbroek: Writing – original draft, Visualization, Validation, Methodology, Investigation, Formal analysis, Data curation. **Christos Georgiadis:** Software, Methodology. **Benoit Scheid:** Validation. **Joris Proost:** Writing – review & editing, Visualization, Validation, Supervision, Methodology, Funding acquisition.

Declaration of competing interest

The authors declare that they have no known competing financial interests or personal relationships that could have appeared to influence the work reported in this paper.

Acknowledgements

Financial support from the Regional Walloon PNRR Project "HeCO2" is gratefully acknowledged. Computational resources have been provided by the supercomputing facilities of the Université catholique de Louvain (CISM/UCL) and the Consortium des Équipements de Calcul Intensif en Fédération Wallonie Bruxelles (CÉCI) funded by the Fond de la Recherche Scientifique de Belgique (F.R.S.-FNRS) under convention 2.5020.11 and by the Walloon Region. B.S. is FNRS Research Director.

Appendix A. Supplementary data

Supplementary data to this article can be found online at https://doi.org/10.1016/j.ces.2025.121513.

Data availability

Data will be made available on request.

References

Kyoto Protocol to the United Nations Framework Convention on Climate Change, Dec. 10, 1997, 2303 U.N.T.S. 162.
Paris Agreement to the United Nations Framework Convention on Climate Change, Dec. 12, 2015, T.I.A.S. No. 16-1104.
The Future of Hydrogen, IEA. https://www.iea.org/reports/the-future-of-hydrogen (accessed Oct. 17, 2022).
Shih, Monteiro, A.J.M.C.O., Dattila, F., Pavesi, D., Philips, M., Silva, A.H.M., Vos, R.E., Ojha, K., Park, S., Heijden, O., Marcandalli, G., Goyal, A., Villalba, M., Chen, X., Gunasooriya, G.T.K.K., McCrum, I., Mom, R., López, N., Koper, M.T.M., 2022. Water electrolysis. Nat Rev Methods Primers 2 (1), 1. https://doi.org/10.1038/s43586-022-00164-0.
Brauns, J., Turek, T., 2020. Alkaline water electrolysis powered by renewable energy: a review. Processes 8 (2), 248. https://doi.org/10.3390/pr8020248.
Li, Y., et al., Jan. 2022. Study the effect of lye flow rate, temperature, system pressure and different current density on energy consumption in catalyst test and 500W commercial alkaline water electrolysis. Materials Today Physics 22, 100606. https://doi.org/10.1016/j.mtphys.2022.100606.
Grigoriev, S.A., Fateev, V.N., Bessarabov, D.G., Millet, P., Oct. 2020. Current status, research trends, and challenges in water electrolysis science and technology. International Journal of Hydrogen Energy 45 (49), 26036–26058. https://doi.org/10.1016/j.ijhydene.2020.03.109.
Proost, J., Jul. 2020. Critical assessment of the production scale required for fossil parity of green electrolytic hydrogen. International Journal of Hydrogen Energy 45 (35), 17067–17075. https://doi.org/10.1016/j.ijhydene.2020.04.259.
Shiva Kumar, S., Himabindu, V., 2019. Hydrogen production by PEM water electrolysis: a review. Materials Science for Energy Technologies 2 (3), 442–454. https://doi.org/10.1016/j.mset.2019.03.002.
Wang, T., Cao, X., Jiao, L., Jun. 2022. PEM water electrolysis for hydrogen production: fundamentals, advances, and prospects. Carb Neutrality 1 (1), 21. https://doi.org/10.1007/s43979-022-00022-8.
Rocha, F., Delmelle, R., Georgiadis, C., Proost, J., Jun. 2022. Effect of pore size and electrolyte flow rate on the bubble removal efficiency of 3D pure Ni foam electrodes during alkaline water electrolysis. Journal of Environmental Chemical Engineering 10 (3), 107648. https://doi.org/10.1016/j.jece:2022.107648.
Rocha, F., Delmelle, R., Georgiadis, C., Proost, J., 2023. Electrochemical performance enhancement of 3D printed electrodes tailored for enhanced gas evacuation during alkaline water electrolysis. Advanced Energy Materials 13 (1), 2203087. https://doi.org/10.1002/aenm.202203087.
Arenas, L.F., Ponce de León, C., Walsh, F.C., Apr. 2017. 3D-printed porous electrodes for advanced electrochemical flow reactors: A Ni/stainless steel electrode and its mass transport characteristics. Electrochemistry Communications 77, 133–137. https://doi.org/10.1016/j.elecom.2017.03.009.
Weusten, S.J.C., Murrer, L.C.E.M., de Groot, M.T., van der Schaaf, J., 2021. Mass transfer in 3D-printed electrolyzers: The importance of inlet effects. AIChE Journal 67 (6), e17263. https://doi.org/10.1002/aic.17263.
Rocha, F., et al., Aug. 2024. Proton exchange membrane-like alkaline water electrolysis using flow-engineered three-dimensional electrodes. Nat Commun 15 (1), 7444. https://doi.org/10.1038/s41467-024-51704-z.
Zhao, P., Wang, J., Sun, L., Li, Y., Xia, H., He, W., Jan. 2024. Optimal electrode configuration and system design of compactly-assembled industrial alkaline water electrolyzer. Energy Conversion and Management 299, 117875. https://doi.org/10.1016/j.enconman.2023.117875.
David, M., Ocampo-Martínez, C., Sánchez-Peña, R., Jun. 2019. Advances in alkaline water electrolyzers: A review. Journal of Energy Storage 23, 392–403. https://doi.org/10.1016/j.est.2019.03.001.
Jang, D., Cho, H.-S., Kang, S., Apr. 2021. Numerical modeling and analysis of the effect of pressure on the performance of an alkaline water electrolysis system. Applied Energy 287, 116554. https://doi.org/10.1016/j.apenergy.2021.116554.
Daoudi, C., Bounahmidi, T., Jan. 2024. Overview of alkaline water electrolysis modeling. International Journal of Hydrogen Energy 49, 646–667. https://doi.org/10.1016/j.ijhydene.2023.08.345.
Zhao, P., Wang, J., He, W., Sun, L., Li, Y., Oct. 2023. Alkaline zero gap bipolar water electrolyzer for hydrogen production with independent fluid path. Energy Reports 9, 352–360. https://doi.org/10.1016/j.egyr.2023.05.135.
Lee, H., et al., Nov. 2021. The Structural Effect of Electrode Mesh on Hydrogen Evolution Reaction Performance for Alkaline Water Electrolysis. Frontiers in Chemistry 9. https://doi.org/10.3389/fchem.2021.787787.
Wang, T., Wang, J., Wang, P., Wang, F., Liu, L., Guo, H., Jan. 2023. Non-uniform liquid flow distribution in an alkaline water electrolyzer with concave-convex bipolar plate (CCBP): A numerical study. International Journal of Hydrogen Energy. https://doi.org/10.1016/j.ijhydene.2022.12.203.
Xue, L., Song, S., Chen, W., Liu, B., Wang, X., 2024. Enhancing efficiency in alkaline electrolysis cells: optimizing flow channels through multiphase computational fluid dynamics modeling. Energies 17 (2), 448. https://doi.org/10.3390/en17020448.
Lafmejani, S.S., Müller, M., Olesen, A.C., Kær, S.K., Sep. 2018. Experimental and numerical study of flow in expanded metal plate for water electrolysis applications.

Journal of Power Sources 397, 334–342. https://doi.org/10.1016/j.jpowsour.2018.07.032.
Rodríguez, J., Amores, E., 2020. Cfd modeling and experimental validation of an alkaline water electrolysis cell for hydrogen production. Processes 8 (12), 1634. https://doi.org/10.3390/pr8121634.
Aboukalam da Cruz, M.H.A., Etancelin, M., Marias, F., Reneaume, J.-M., Sochard-Reneaume, S., Serra, S., Apr. 2023. Dynamic modelling of an alkaline water electrolysis system and optimization of its operating parameters for hydrogen production. International Journal of Hydrogen Energy 48 (35), 12982–12999. https://doi.org/10.1016/j.ijhydene.2022.12.130.
Lee, J., Alam, A., Park, C., Yoon, S., Ju, H., May 2022. Modeling of gas evolution processes in porous electrodes of zero-gap alkaline water electrolysis cells. Fuel 315, 123273. https://doi.org/10.1016/j.fuel.2022.123273.
El-Askary, W.A., Sakr, I.M., Ibrahim, K.A., Balabel, A., Oct. 2015. Hydrodynamics characteristics of hydrogen evolution process through electrolysis: Numerical and experimental studies. Energy 90, 722–737. https://doi.org/10.1016/j.energy.2015.07.108.
Wosiak, G., da Silva, J., Sena, S.S., de Andrade, R.N., Pereira, E., Apr. 2022. CFD simulation and experimental comparison of bubble-induced convection during electrochemical water splitting. Chemical Engineering Journal 433, 133194. https://doi.org/10.1016/j.cej.2021.133194.
Rajora, A., Haverkort, J.W., Aug. 2023. An analytical model for the velocity and gas fraction profiles near gas-evolving electrodes. International Journal of Hydrogen Energy 48 (71), 27450–27463. https://doi.org/10.1016/j.ijhydene.2023.03.154.
Le Bideau, D., Mandin, P., Benbouzid, M., Kim, M., Sellier, M., Feb. 2019. Review of necessary thermophysical properties and their sensivities with temperature and electrolyte mass fractions for alkaline water electrolysis multiphysics modelling. International Journal of Hydrogen Energy 44 (10), 4553–4569. https://doi.org/10.1016/j.ijhydene.2018.12.222.
Sakas, G., Ibáñez-Rioja, A., Ruuskanen, V., Kosonen, A., Ahola, J., Bergmann, O., Jan. 2022. Dynamic energy and mass balance model for an industrial alkaline water electrolyzer plant process. International Journal of Hydrogen Energy 47 (7), 4328–4345. https://doi.org/10.1016/j.ijhydene.2021.11.126.
Sakas, G., et al., Apr. 2024. Sensitivity analysis of the process conditions affecting the shunt currents and the SEC in an industrial-scale alkaline water electrolyzer plant. Applied Energy 359, 122732. https://doi.org/10.1016/j.apenergy.2024.122732.
Batchelor, G.K., 1967. An Introduction to Fluid Dynamics. Cambridge University Press.
Lee J.H.W. Chu V.H. Lee J.H.W. Chu V.H. Turbulent jets and plumes: a Lagrangian approach 2003 Springer US Boston, MA 21 54 10.1007/978-1-4615-0407-8_2 , pp.
Zuckerman N. Lior N. Greene G.A. Hartnett J.P. Bar-Cohen A. Cho Y.I. Advances in heat transfer 2006 Elsevier 565 631 10.1016/S0065-2717(06)39006-5 , pp.
Kuhlmann, K., Sinn, C., Siebert, J.M.U., Wehinger, G., Thöming, J., Pesch, G.R., Dec. 2022. From μCT data to CFD: an open-source workflow for engineering applications. Engineering Applications of Computational Fluid Mechanics 16 (1), 1706–1723. https://doi.org/10.1080/19942060.2022.2109758.
Sadeghi, M., Mirdrikvand, M., Pesch, G.R., Dreher, W., Thöming, J., May 2020. Full-field analysis of gas flow within open-cell foams: comparison of micro-computed tomography-based CFD simulations with experimental magnetic resonance flow mapping data. Exp Fluids 61 (5), 124. https://doi.org/10.1007/s00348-020-02960-4.
Edouard, D., Lacroix, M., Huu, C.P., Luck, F., Oct. 2008. Pressure drop modeling on SOLID foam: State-of-the art correlation. Chemical Engineering Journal 144 (2), 299–311. https://doi.org/10.1016/j.cej.2008.06.007.
Liu, J.F., Wu, W.T., Chiu, W.C., Hsieh, W.H., Mar. 2006. Measurement and correlation of friction characteristic of flow through foam matrixes. Experimental Thermal and Fluid Science 30 (4), 329–336. https://doi.org/10.1016/j.expthermflusci.2005.07.007.
Probstein, R.F., 2005. Physicochemical Hydrodynamics: An Introduction. John Wiley & Sons.
Tham, M.J., Walker Jr., R.D., Gubbins, K.E., 1970. Diffusion of oxygen and hydrogen in aqueous potassium hydroxide solutions. J. Phys. Chem., 74 (8), 1747–1751. https://doi.org/10.1021/j100703a015.
Li, S., 2017. Reaction Engineering. Butterworth-Heinemann.
Nauman, E.B., 2003. 'Residence Time Distributions', in Handbook of Industrial Mixing. John Wiley & Sons, Ltd 1–17. https://doi.org/10.1002/0471451452.ch1.
M. Ishii T. Hibiki Thermo-Fluid Dynamics of Two-Phase Flow 2011 Springer New York, NY 10.1007/978-1-4419-7985-8.
Innocentini, M.D.M., Salvini, V.R., Macedo, A., Pandolfelli, V.C., Oct. 1999. Prediction of ceramic foams permeability using Ergun's equation. Mat. Res., 2, 283–289. https://doi.org/10.1590/S1516-14391999000400008.